

**Comparative study of wall shear stress at the ascending aorta for different
mechanical heart valve prostheses**

Qianhui Li and Christoph H. Bruecker

School of Mathematics, Computer Science and Engineering. City, University of
London, Northampton square, London, EC1V 0HB, UK

Abstract

An experimental study is reported which investigates the wall shear stress (WSS) distribution in a transparent model of the human aorta comparing a bileaflet mechanical heart valve (BMHV) with a trileaflet mechanical heart valve (TMHV) in physiological pulsatile flow. Elastic micro-pillar WSS sensors, calibrated by micro-Particle-Image-Velocimetry measurement, are applied to the wall along the ascending aorta (AAo). Peak WSS values are observed almost twice in BMHV compared to TMHV. Flow field analyses illuminate that these peaks are linked to the jet-like flows generated in the valves interacting with the aortic wall. Not only the magnitude but also the impact regions are specific for the different valve designs. The side-orifice jets generated by BMHV travel along the aortic wall in the AAo and cause a whole range impact, while the jets generated by TMHV impact further downstream in the AAo generating less severe WSS.

Keywords: aortic valve flow, PIV, wall shear stress, micro-pillar sensors

1. Introduction

Most disorders of the heart are initiative in the left ventricle due to the highest mechanical loads which are subjected to this chamber.[1] The mitral and the aortic

valve regulate the flow of oxygenate blood to the body through the left ventricle and determine the inflow and outflow conditions, which are the most commonly affected heart valves in a diseased heart, responsible for 34% and 44% of morbidity respectively.[2, 3] Although prevalence of the heart valve disease (HVD) is low compared with coronary heart disease, the requirement for long-term follow-up, and significant investigation and treatment costs, means that the impact of HVD on healthcare systems is disproportionately large.[4] Concomitantly, the annual number of patients requiring heart valve replacement is estimated to triple from approximately 290,000 in 2003 to over 850,000 by 2050.[5] It has been reported that artificial heart valves replacement has been associated with a variety of valve-related complications often leading to serious disability or death.[6] One main reason is that hemodynamics induced by artificial heart valves is different from the natural valve. There is a huge requirement to better qualify hemodynamics performance of artificial heart valves and make improvement in the design. Fluid mechanics of artificial heart valve has attracted extensive attention in the past, for review papers see Sotiropoulos et al. [7] and Yoganathan et al. [3]. The additional jets that emanate from these prostheses usually generate high-velocity gradients and inhomogeneous flow that exceed those in the natural valve.[8] In addition to the core flow, the jet-wall interaction in the aorta is also of importance, since high-velocity gradients, i.e. high magnitude of wall shear stress (WSS), in the impacting region are formed. WSS provides a connection between the fluid mechanics of blood flow and the biology affecting many cardiovascular diseases. Oscillating shear forces plus large WSS gradients probably promote the development of intimal hyperplasia (IH).[9]

Moreover, a high WSS could cause sublethal or lethal damage in the endothelial cells of the aorta.[10, 11] Besides, aortic aneurysm rupture is believed to occur when the mechanical stress acting on the wall, composed of pressure forces and the WSS, exceeds the strength of the wall tissue.[12] It has also been reported that vessel segments with low WSS or highly oscillatory WSS appear to be at the highest risk for development of atherosclerosis. WSS mapping may someday become part of the multifactorial, multidisciplinary approach to early atherosclerosis detection.[13]

It is obvious that there is a need for a specific analysis of the valve design with respect to the generated flow structures and their interaction with the vessel walls to qualify the valve performance. Also, the measurement of WSS in the aorta is important to understand the exposure of the endothelial cells to stress along the aortic wall. Although it has been reported that the oscillation, low or high magnitude of the WSS can lead to severe heart diseases,[10, 11] to our knowledge, most of the previous studies[1, 8, 14] on the qualification of the artificial valves mainly focus on the flow field in the vicinity of artificial valves in simplified straight vessel models. Only very little attention is paid to the effects of the implanted artificial heart valves on WSS magnitude and distribution along the aortic wall.[15] As for measurement methods, there are quite a lot of limitations to perform measurements in a natural condition, as the test section are organs in vivo and the fluid is blood. The limited spatial resolution of the in-vivo measurements such as magnetic resonance imaging (MRI)[16] leads to huge challenge to measure WSS accurately. Also, it is high-risk to qualify a newly designed artificial heart valve by implanting it into a human body. The in-vitro measurement such as Particle Image Velocimetry (PIV) still require optical access. It is

also difficult to apply direct measurements by using MEMS or other WSS sensors to such studies. In our study, we applied flexible micro-pillar sensors, for the first time, to imaging of the wall shear stress along the AAo. The micro-pillar sensors have a broad application prospect, they could be even applied to a non-transparent fluid such as blood if markers are attached to the sensor tips. Calibration is done herein with highly resolved PIV measurements in a transparent flow rig.

2. Materials and Methods

Heart valve prosthesis

Artificial heart valves are divided into two major types, mechanical heart valves (MHV) and bioprosthetic heart valves. Until recently, heart valve replacement was commonly performed using MHV, which offer a life-long durability.[17] We herein focus on the comparative study of MHV, including SJM Regent BMHV (St. Jude Medical Inc., Minnesota, U.S.) and Triflo TMHV (Triflo Medical Inc., Neuchâtel, Switzerland) with the same diameter $D_A = 25$ mm (see Fig. 1). SJM Regent valve is a widely used MHV and therefore taken as a control valve in our comparative study. Nonetheless, clinical reports indicate that conventional MHV are still unable to eliminate the problems of thrombosis and complications on the long-term anticoagulation.[6] Triflo TMHV consists of three leaflets that open to form a central orifice for the blood to flow through and three side orifices jets. The design of TMHV more closely resembles the native aortic valves and is assumed to have a better hemodynamics performance. An open circular orifice nozzle is also used to perform in-situ micro-PIV measurements for the calibration of the micro-pillar sensors.

Experimental setup

The geometry data of the model aorta are taken from Vasava et al.[18], who simplified the geometry derived from the three-dimensional reconstruction of a series of two-dimensional slices obtained in vivo using CAT scan imaging on a human aorta by Shahcheraghi et al. [19] (see table 1). Although the geometrical dimensions of human aorta may slightly vary with age and sex, the comparative effects observed between the bileaflet mechanical heart valve (BMHV) and the trileaflet mechanical heart valve (TMHV) should represent the relative differences in a realistic manner. The diameter of the aorta is $D_A=25\text{mm}$ and the MHVs are selected to properly fit the size. The 180° curved bend representing the aortic arch with sinuses of Valsalva (SOV) has a planar symmetry plane (crossing the left sinus in the middle), which is useful for our model fabrication and sensor integration. A transparent model consisting of two symmetric halves is casted out of transparent silicone (Elastosil RT 601™, refractive index $n \approx 1.4095$) following the method described by Triep et al.[20]. A negative form of the aorta shown in Fig. 2(b) is created using a casting mould (Resinpal 1707, Fiberglas Discount GmbH, Fahrenzuhausen, Germany) in Fig. 2(a). From this negative form two symmetric halves are casted from silicone as positives, which are later assembled together as shown in Fig. 2(d). A thin sheet with thickness of $100\text{ }\mu\text{m}$ is clamped between both halves and carries twelve flexible micro-pillars made from Polydimethylsiloxane (PDMS) (density $\rho_{PDMS} \approx 1030\text{ kg}\cdot\text{m}^{-3}$, Young's modulus $E \approx 1.24\text{ MPa}$) (see Fig. 2(c)). The curved contour of the sheet is adapted to the geometry of the inner wall of the model such that it is flush with the wall with the flexible micro-pillars protruding into the inner of the flow. There, the micro-pillars are

subject to drag forces proportional to the WSS, which causes their bending relative to the situation when the liquid is at rest.

Artery properties	Dimension (mm)
(1) Diameter of sinus bulb	21
(2) Ascending and descending aorta lumen diameter	25
(3) Brachiocephalic artery (BA) lumen diameter	8.8
(4) Left common carotid artery (LCA) lumen diameter	8.5
(5) Left subclavian artery (LSA) lumen diameter	9.9

Table 1. Main dimensions of the aorta geometry, taken from Vasava et al.[18].

Measurements of the flow inside the aorta are carried out with the transparent model submerged in a transparent glass basin (width/depth: 190 mm, height: 500 mm) and using as working liquid a glycerine-water solution (58/42 % by mass, density $\rho = 1140 \text{ kg m}^{-3}$, dynamic viscosity $\mu = 5 \text{ mPa}\cdot\text{s}$ at the temperature of 38°C , refractive index 1.4095). The matching of the refractive index is essential for avoiding optical distortions and for achieving a good image quality of the PIV recordings in regions close to the aortic wall, see Fig. 2(e). Small tracer particles (fluospheres, mean diameter 30micron, Dantec Dynamics) are added to the liquid for the PIV recordings during sensor calibration and flow studies. Although the working liquid in our study shows a Newtonian behaviour, it has been proven that blood behaviour can also be approximated as Newtonian if the flow considered is in vessels with diameter larger than 1 mm as pointed out in former studies.[21, 22] A newly developed PIV plasma

with rheological and coagulation properties has been reported by Clauser et al.[23].

The viscosity used in our study is the upper range of their study.

The MHVs are mounted at the sinus root in the centre of the fluid basin (see Fig. 3(a)) such that in both cases the left-most leaflet is facing the left sinus in the symmetry-plane. For the Triflo TMHV the other leaflets face then the direction of the other sinus bulbs too, while for the SJM Regent the right leaflet is in the middle of both. For reference measurements, a thin-walled nozzle with circular orifice (outer diameter 25mm, inner diameter 24.6mm) was inserted into the aorta in the same plane as the MHV, which blocks the region of the SOV and generates a smooth core flow into the aorta. This configuration is studied at the same physiological flow rate for calibration of the sensors with simultaneous micro-PIV measurements.

A transparent inlet tube is placed upstream of the MHVs, which is connected to a pulse flow generator by a flexible pipe. A linear actuator (MOOG, AC-Servo-Actuator, Böblingen, Germany) generates a physiological pulsatile flow, with a heart rate of 70 per minute and a stroke volume of 80ml. Each cycle, including systole and diastole period, has a duration of 850 ms, see Brücker et al.[24]. To represent a typical systolic heart pressure a hydrostatic liquid height of 170 mm above the heart valve level was imposed, supported by an additional air overpressure applied on top of the basin.

Time-resolved particle image velocimetry (TR-PIV)

A continuous wave Argon-Ion laser (Raypower 5000, 5 W power at $\lambda = 532$ nm, Dantec Danamics) is used as illumination source. The output laser beam is about 1.5 mm in diameter and is further expanded to a sheet illuminating the symmetry plane of the

aorta. Full format recordings of the flow in the AAo are done with a high-speed camera (Phantom Miro 310, Ametek, 576×768 px² recording at 7200 fps) equipped with a lens (Tokima Macro $f=100\text{mm}$, F 2.8) showing a field of view of 57.6 x 76.8 mm² (see Fig. 4(b)). Zoomed-in recordings are carried out by using a 2x teleconverter (TC 20, Nikon, Chiyoda, Tokio, Japan) and a long-distance microscope (Model K2/SC™, Infinity Photo-Optical Company, Boulder, USA) reaching a field of view of 4.0 x 6.4 mm² at 7200 fps, which is used for the recording of the micro-pillars during calibration with simultaneous micro-PIV measurements.

The post-processing to capture the pillar tip motion and the flow field is done with an in-house Matlab code. For PIV, the images are masked within the pillar regions and processed with 2D cross-correlation of successive images to calculate the in-plane velocity vector fields. Processing is done in small interrogation windows with an iterative grid refinement method with final window size of 32x32 px². To illustrate the trajectory patterns of the jets in the flow the finite-time Lyapunov exponent (FTLE) is calculated from the velocity fields (LCS MATLAB Kit Version 1.0, Dabiri Lab, Stanford University). This has been proven as an efficient diagnostic tool for time-evolving patterns in dynamical systems as it allows tracking of Lagrangian coherent structures (LCSs) represented by the largest values in the FTLE field. [25] The calculation is done backward in time with a time interval of 14 ms for 10 snapshots with an interval of 10 snapshots.

Wall shear stress imaging

For measuring the wall shear stress, the method of flexible micro-pillar sensors developed by Brücker et al.[26] is implemented, a sketch of which is shown in Fig. 4(a). The static and dynamic response of these sensors is characterized for different pillar shapes and fluids in our previous studies.[27, 28] The following assumptions hold for the current flow situation: a) the density of the pillar is in the same order as the density of the liquid such that gravitational forces play no role in the pillar motion; b) due to the small scale of the sensors the local Reynolds-number $Re_{Tip} = \rho U_{Tip} d / \eta$ is of order $O(10)$ which is in the linear regime of viscous fluid structure interaction without any vortex shedding; c) the velocity profile close to the wall can be approximated to first order as linear $u(y) = U_{Tip} y / l + O(\varepsilon)$ up to the length of the pillar with the characteristic velocity U_{Tip} at the tip of the pillar; d) bending is small compared to the length of the pillars and therefore wall-normal forces are only of second-order influence compared to the wall-parallel shear; e) the time scale of sensor relaxation $\tau \approx 5$ ms is small compared to the characteristic time-scale $T_{sys} = 386$ ms of the flow. To compare it with the temporal Kolmogorov scale, a typical pressure drop $\Delta p = 1000$ Pa of MHVs over a segment of flow of length $L = D_A$ is selected, the dissipation rate per unit of mass can be estimated as

$$\varepsilon = \frac{\Delta p Q}{\rho V} \approx 6.67 \text{ W} \cdot \text{kg}^{-1} \approx 6.67 \text{ m}^2 \cdot \text{s}^{-3} \quad (1)$$

where $Q = U_m \pi D_A^2 / 4$ is the flow rate and $V = L \pi D_A^2 / 4$ is the volume of the segment.

The temporal and spatial Kolmogorov scales are defined according to [29] by

$$\tau_K = \left(\frac{\nu}{\varepsilon}\right)^{1/2}, \eta_K = \left(\frac{\nu^3}{\varepsilon}\right)^{1/4} \quad (2)$$

respectively, where $\nu = \mu/\rho$ is the kinematic viscosity. Thus, the Kolmogorov scales for the considered aortic flow in our study are estimated to be $\tau_K \approx 0.8 \text{ ms}$ and $\eta_K \approx 60 \text{ }\mu\text{m}$. However, our focus is on oscillations in WSS that are induced by coherent flow structures, which are typically more than one order of magnitude larger in spatial and temporal scales. Previous studies confirmed that the important characteristics of heart valve flows is the dominance of large-scale coherent structures over any random fluctuations due to turbulence.[7] For the micro-pillar sensors applied herein, it is further assumed that only the low-frequency range portion persists within the very near-wall region, which is associated with the near-wall dynamics of the coherent vortex structures.[26]

Under the above given assumptions the micro-pillar tip bending is then direct proportional to the wall shear rate with a constant response up to frequencies of about 200Hz [27, 28]. The proportionality factor is obtained in a calibration test under the same pulsatile flow conditions in the aortic arch where the micro-pillars are recorded simultaneous with micro-PIV measurements, in which the tip's displacement along the wall is calibrated by the wall-normal gradient of the tangential velocity.

The micro-pillar sensors labelled from 1 to 12 are placed uniformly along the outer aortic wall in the AAo (see Fig. 3(b)) in the middle between both model halves. The symmetry plane is where the flow is documented most of the time to be 2D with only weak out-of-plane motion, also seen from the original particle recordings by the long residence time of the particles in the light-sheet plane. We expect in this region peak

values in WSS in streamwise direction when the side-orifice jets emanating from the gap between the valve ring and leaflets impact with the aortic wall. Two exemplary sensor locations are selected for the presentations of the results, one in the upstream region at pillar #4 and one in the downstream region at pillar #11. The tip displacement of micro-pillar sensor is detected with sub-pixel resolution (optical measurement uncertainty $<0.1\text{px}$, maximum tip displacement 10px). A second order low-pass filter with cut-off frequency of 200Hz is used to reduce measurement noise above the frequency response of the sensor.

The measured tip displacement relative to the situation with liquid at rest is converted into the wall shear rate by calibration with the simultaneous micro-PIV recording, carried out in the open circular orifice configuration. The sketch of micro-PIV data processing is shown in Fig. 4(b). The cross-correlation of successive images is performed with a window size of $240 \times 64 \text{ px}^2$ and 75% overlap. The velocity profile at near wall region calculated from the micro-PIV recording is plotted in Fig. 4(c), from which a liner curve-fit is generated. The slope of the liner curve-fit is the value of the instantaneous streamwise velocity gradient at the wall, i.e. the wall shear rate. The peak value in the time-series of the PIV measurements is used to determine the proportionality constant. The comparative plots of the wall shear rate distribution over the systolic cycle (see Fig. 4(d)) show that the time-resolved micro-pillar signal coincides well with the results of the micro-PIV measurement. At the end of systolic cycle, the downstream near wall flow field is quite complex and often not enough tracer particle remain in the interrogation window which is why the micro-PIV data fail in the valve closure phase. Note, that imaging of the WSS distribution can be done

simultaneous for 4-8 micro-pillar sensors while for the micro-PIV measurements very high seeding densities are required to get good PIV results near the wall, which is often not possible due to strong reflections and particle migration to the core flow away from strong near-wall velocity gradients. This is why WSS measurements using the micro-pillar sensors are ideally suited for complex flows as expected in the valve studies.

3. Results

Inlet flow condition and leaflet kinematics

The inlet flow profile is shown in see Fig. 5(a), with a systolic heart beat duration of $T_{sys}=386$ ms characterised by acceleration flow phases from 0 to $0.2T_{sys}$, peak systole phase from $0.2T_{sys}$ to $0.4T_{sys}$, deceleration flow phases from $0.4T_{sys}$ to $0.9T_{sys}$, and valve closure phases from $0.9T_{sys}$ to T_{sys} . At the peak of the flow, the peak inlet velocity reaches a value of $U_p = 0.95 \text{ m}\cdot\text{s}^{-1}$. The mean velocity averaged over the complete beat cycle amounts to $U_m = 0.19 \text{ m}\cdot\text{s}^{-1}$. The non-dimensional physical parameters of the flow are represented by the Reynolds number, Strouhal number and Womersley number:

$$Re_p = \frac{\rho U_p D_A}{\mu}, St = \frac{D_A}{2} \frac{f}{(U_p - U_m)}, \alpha = \frac{D_A}{2} \sqrt{\frac{2\pi f \rho}{\mu}}, \quad (3)$$

where f is the heart rate. It is obtained that $Re_p = 5340$, $St = 0.019$ and $\alpha = 16$.

The critical peak Reynolds number is calculated according to [30] based on the measured Strouhal number and Womersley number according to $Re_p^c = 169\alpha^{0.83}St^{-0.27}$, from which we obtain $Re_p^c = 4925$. The supracritical Reynolds

number is $Re_p - Re_p^c = 415$, which indicates that the flow is unstable.[30] Also, as the non-dimensional physical parameters of the flow are similar to that observed in in-vivo experiment of the healthy aorta performed among 30 volunteers by Stalder et al. [30], it indicates that the flow condition used in our study is representative for the natural flow situation.

The flow measurements are supplemented by instantaneous positions of both leaflets of BMHV and of TMHV, taken from high speed recordings of the tip motion of the leaflets. Note, that all three leaflets of TMHV open and close simultaneously and therefore one profile is representative for all other leaflets.[24] Comparative results of the leaflet motion measurements are given in Fig. 5(b). The leaflets of TMHV reach a maximum opening position at an angle of about 75° after $0.1T_{sys}$, while the leaflets of BMHV reach the maximum angle of 85° at $0.2T_{sys}$. The leaflets of BMHV are observed to have a different start in closing related to the orientation of the leaflets relative to the sinuses, i.e. the left leaflet facing the left sinus closes later at $0.8T_{sys}$ while the right leaflet starts closing much earlier at $0.6T_{sys}$.

Flow field

Analysis of the velocity field is done by calculating the out-of-plane component of the vorticity by central difference scheme and displaying those as color-coded iso-contours overlaid with the velocity vector field in Fig. 6, with a comparison of flow evolution for the BHMV compared to TMHV. Further analysis by the FTLE field shown in Fig. 7 illustrates the jet pattern generated by both MHVs. Regions of high FTLE values allow to recognize the boundaries of the jets. In addition, regions of high

vorticity near the wall let recognize the development of the boundary layers along the walls.

SJM Regent BHMV. During the valve opening phase (see Fig. 6(a)), the leaflets' leading edges move from outside towards the center. A pair of vortices occur at the outer edges of the leaflets by shear layer separation, marked as outer starting vortices in Fig. 6(a). Flow separation at the edge of the valve housing causes the anti-clockwise vortex penetrating into the left sinus region, which is the so-called aortic sinus vortex (ASV). These vortices affect the near wall flow in the aorta while they travel further up into the AAo (see Fig. 6(b)). Later, regular rows of discrete vorticity structures occur downstream of the leaflets with alternating sign, resembling the form of von Karman-type vortex streets.

The boundary between fluid entering into the aorta from the fluid inside the aorta above the valve is presented high FTLE values, see in the region of the left sinus in Fig. 7(a) and (d). A wash-out flow driven by the ASV can be observed and the generation of the left side orifice jet is seen in Fig. 7(b). Downstream of the trailing edges of both leaflets the above discussed vortex streets appear as vertical columns with a zig-zag type pattern of the shear layers. At peak systole shown in Fig. 7(c), the SOJ has attached to the left wall of the aorta and affects the outer aortic wall.

Triflo TMHV. In the opening phase of the Triflo, the tips of the leaflet move from the center towards the sinuses, which causes a different flow field than in SJM. A leading inner starting vortex is followed by an outer starting vortex when the left leaflet reaches the maximum opening position. Both travel further downstream while in the inner part of the valve the central jet builds up, seen by rather uniform core flow in

Fig. 6(e) and (f).

The more significant high FTLE value shown at the left sinus region in Fig. 7(d) indicates that there is a stronger wash-out flow compared to BMHV, which is supported by the displacement fluid generated by of the outwards rotating leaflet. The separated shear layers at the outer and inner edge of the leaflet are presented by the side orifice jet and central orifice jet separately. Thereafter, these two jets mix together and travel towards the centre of the aorta instead of impacting on the vessel wall at peak systole (see Fig. 7(e) and (f)).

Besides, the absolute value of out-of-plane vorticity field is integrated across the entire flow field and normalized by the open orifice nozzle configuration, which gives a rough quantitative indication how chaotic the flow is due to extra vorticity generated in the jets and wakes of the valve-ring and occluders. The normalized integration of BMHV is $E_{BMHV} = 1.93$ at $0.18T_{sys}$, $E_{BMHV} = 1.49$ at $0.25T_{sys}$ and $E_{BMHV} = 1.45$ at $0.4T_{sys}$ over peak systole phase. Compared to BMHV, the normalized integration of TMHV leads to values of $E_{TMHV} = 1.94$ at $0.18T_{sys}$, $E_{TMHV} = 1.34$ at $0.25T_{sys}$ and $E_{TMHV} = 1.27$ at $0.4T_{sys}$. This indicates that the flow field is more chaotic in BMHV over peak systole phase. Note that this is obtained only from a single plane in the flow and therefore the conclusion may not necessarily holds for the entire flow field. Though, as this plane is the symmetry plane of the flow crossing the centre of the shear layers it is a strong indicative for the entire flow.

Wall shear rate

Comparative profiles of wall shear rate in BMHV, TMHV and open circular orifice nozzle configurations are presented for the systolic cycle. The circular orifice configuration can be regarded as a reference flow in the arch at identical physiological flow conditions as for the MHVs, but without the influence of valve bodies. The profiles of wall shear rate measured by the micro-pillar sensors at upstream region and downstream region are plotted in Fig. 8(a) and (b), respectively.

During the valve opening phase, the flow acceleration generates a progressive rise of the wall shear rate with similar shape for all configurations. In this early phase, the displacement effect generated by the opening valves is similar for all configurations and the WSS is mainly influenced by bulk flow movement. The measured profiles resemble in this phase strongly those of the reference flow without a valve. Thereafter, BMHV shows a further increase of wall shear rate, which is linked to a stronger wash-out flow from the side orifice jet. At around $0.2T_{sys}$, a drop is seen for both MHVs. This is caused by the passing-by of the counter-clockwise-rotating vortex structure of the inner starting vortex which temporarily induces a reduction of the near-wall flow velocity.

Shortly thereafter, a large positive peak of the wall shear rate appears around the peak systole in BMHV, which is caused by the impact of the strong side orifices jet-like flow travelling the outer aortic wall in the AAo. The peak wall shear rate reaches 2123 s^{-1} in BMHV while the peak wall shear rate in TMHV configuration is only 910 s^{-1} , which is less than half of the BMHV and of similar magnitude as observed for the reference case.

After this peak, the profiles show characteristic waviness in the temporal signal which is due to the quasi-periodic shear-layer roll-up in the region between the core flow and the wall while global flow starts to decelerate. It can also be found that the waviness is larger in BMHV compared with the TMHV, which means the rolling-up of the shear layer along the outer aortic wall in the AAo of BMHV is more intense. This phenomenon is more significant at further downstream region of BMHV (see Fig. 8(b)) from $0.35T_{sys}$ to $0.6T_{sys}$. Moreover, the peak wall shear rate of BMHV is 2046 s^{-1} , which is still twice the value of the peak wall shear rate of TMHV in this region, i.e. 1030 s^{-1} .

4. Discussion and Conclusion

Our detailed experimental results of the flow field generated by BMHV in the aortic arch can be compared to previous studies by Dasi et al.[8] and De Tullio et al.[14] at similar non-dimensional flow parameters and inlet flow profiles. As we use a more realistic curved geometry of the arch compared to the straight axisymmetric aorta of Dasi et al., we observed almost an asymmetric flow. The left leaflet of BMHV facing directly the sinus is delayed in closing due to the HV, while the two leaflets in the study of Dasi et al. show a synchronous motion when closing. The leaflet motion applied in the numerical study performed by De Tullio et al. coincides with our results, as well as the structure of the asymmetric flow field supporting our flow field results. This also means the curved geometry of the aortic arch is important to recover the impact of flow structures on the aortic walls, which is the reason for high peaks in WSS.

During valve opening, a strong wash-out flow at SOV is observed in TMHV. It indicates that, compared to BMHV, TMHV has a better performance on assisting blood transportation to coronary arteries, which helps with blood supply to the heart muscle.

In addition, the zig-zag type flow pattern representing the vortex streets in the wake of the leaflets of BMHV is not observed in TMHV configuration. Rather, the latter shows a more homogeneous core flow with less small-scale structures generated in the shear layers. Besides, the side orifice jet of BMHV impacts on the outer wall of the AAo and causes peak WSS values with about three-fold magnitude compared to the reference flow at the same inlet flow profile. In comparison, the results of TMHV show that the impact of orifice jets generated by TMHV is much weaker as for the BMHV. A first small peak WSS appears at the same time for both MHVs and for the reference flow, which is induced by the initial wash-out flow. Shortly thereafter, the jet-like flow generated by BMHV impacts on the outer aortic wall, causing a steep increase to high peaks of WSS. As the side orifice jet of BMHV propagates earlier into the aorta than the central orifice jet, the WSS signal shows the maximum peak earlier in time than the TMHV. In comparison, the later peak in THMV is caused by the central jet impacting further downstream the aortic wall. This indicates that not only the magnitude of mechanical force, but also the impact regions are specific to the different valves designs.

The numerical simulation of the flow in the human aorta by Lantz et al.[31], based on MRI-acquired geometry and flow rate of a subject specific aorta, shows a similar peak wall shear rate of about 800 s^{-1} in the downstream region for a natural valve compared to our open orifice nozzle configuration at similar pulsatile flow (reference flow). In addition, their comparative study of a rigid aorta with a flexible one using fluid-structure interaction (FSI) has proven that there is only a small difference in terms of the magnitude of the instantaneous WSS in the AAo. This shows that our WSS

measurements provide reliable values although our model neglects flexible walls. When transferring the shear rates into stresses by multiplying with the dynamic viscosity, the mechanical forces along the aortic wall reach peak stresses of roughly $100 \text{ dyn}\cdot\text{cm}^{-2}$ for BMHV and only half about that for TMHV compared to the reference case with about $40 \text{ dyn}\cdot\text{cm}^{-2}$. These values are still about one order of magnitude larger than the WSS values reported by Meierhofer et al[16] obtained in an in-vivo MRI study of the flow in the AAo. However, it is not clear if their reported values are averages along the circumference of the walls. In general, the spatial resolution of MRI of about 1mm is not sufficient to capture the steep velocity gradients near the wall, therefore we assume a strong underestimation of the true WSS. However, while their absolute magnitude of WSS values might be much too low, the comparative effects observed between tricuspid and bicuspid aortic valves should represent the relative differences in a realistic manner. Their results showed a 15% higher WSS in the AAo for patients with bicuspid aortic valve caused by inborn connective tissue disease compared to the natural tricuspid aortic valves. They concluded that this increase is correlated with the often-observed dilation of the aorta in such patients. Transferring this conclusion to our comparative WSS measurements it indicates that TMHV may have the potential to largely reduce mechanical forces on the aortic walls compared to the standard mechanical prostheses having only two leaflets.

In summary, the main focus of our study is to investigate the mechanical load imposed by WSS along the vessel wall in the AAo when MHV prostheses are implanted. Our study describes, for the first time, direct time-resolved WSS measurements with an array of sensors distributed along the curved aortic wall, by which we investigate the

effects of MHVs on WSS distribution. The technique of micro-pillar WSS imaging is applied to achieve details of the shear stress working on the blood cells near the wall regions and the endothelial cells during a whole systolic cycle, which normally is very difficult to achieve. The results show the peaks in WSS located with the impact regions of the valve-specific orifice jets.

5. Acknowledgements

This work was sponsored by BAE System and the Royal Academy of Engineering (RCSRF1617\4\11), both jointly funding the position of Professor Christoph Bruecker, which is gratefully acknowledged herein. The position of MSc Qianhui Li was supported by the German Research Foundation in the grant DFG 1494/32-1 which is also gratefully acknowledged. We thank the Helmholtz Institute of RWTH Aachen University for providing us the SJM Regent valve and Didier Lapier for the Triflo valve.

6. Funding

BAE System

Royal Academy of Engineering (RCSRF1617\4\11)

German Research Foundation (DFG 1494/32-1)

7. References

- [1] Barannyk, O. and Oshkai, P., 2015, "The influence of the aortic root geometry on flow characteristics of a prosthetic heart valve," *J. Biomech. Eng.*, 137(5), p. 051005.
- [2] Iung, B., Baron, G., Butchart, E.G., Delahaye, F., Gohlke-Bärwolf, C., Levang, O.W., Tornos, P., Vanoverschelde, J.L., Vermeer, F., Boersma, E., and Ravaud, P., 2003, "A prospective survey of patients with valvular heart disease in Europe: The Euro Heart Survey on Valvular Heart Disease," *Eur. Heart. J.*, 24(13), pp. 1231-1243.
- [3] Yoganathan, A.P., He, Z., and Jones, S. C., 2004, "Fluid mechanics of heart valves," *Annu. Rev. Biomed. Eng.*, 6, pp. 331-362.
- [4] Coffey, S., Cairns, B.J. and Iung, B., 2015, "The modern epidemiology of heart valve disease," *Heart.*, pp. heartjnl-2014.
- [5] Yacoub, M. H. and Takkenberg, J. J. M., 2005, "Will heart valve tissue engineering change the world?," *Nature a-z index.*, 2(2), pp. 60-61.
- [6] Fernandez, J., Laub, G.W., Adkins, M.S., Anderson, W.A., Chen, C., Bailey, B.M., Nealon, L.M. and McGrath, L.B., 1994, "Early and late-phase events after valve replacement with the St. Jude Medical prosthesis in 1200 patients," *The Journal of thoracic and cardiovascular surgery.*, 107(2), pp. 394-407.
- [7] Sotiropoulos, F., Trung B. L., and Anvar G., 2016, "Fluid mechanics of heart valves and their replacements.," *Annual Review of Fluid Mechanics*, 48, pp. 259-283.
- [8] Dasi, L.P., Ge, L., Simon, H.A., Sotiropoulos, F. and Yoganathan, A.P., 2007, "Vorticity dynamics of a bileaflet mechanical heart valve in an axisymmetric aorta," *Phys. Fluids.*, 19(6), p. 067105.
- [9] Haruguchi, H. and Teraoka, S., 2003, "Intimal hyperplasia and hemodynamic factors in arterial bypass and arteriovenous grafts: a review," *J. Artif. Organs.*, 6(4), pp. 227-235.
- [10] Walker, P.G. and Yoganathan, A.P., 1992, "In vitro pulsatile flow hemodynamics of five mechanical aortic heart valve prostheses," *Eur. J. Cardio-Thorac.*, 6(Supplement_1), pp. S113-S123.
- [11] Marsden, A.L., Bazilevs, Y., Long, C.C. and Behr, M., 2014, "Recent advances in computational methodology for simulation of mechanical circulatory assist devices," *Wires. Syst. Biol. Med.*, 6(2), pp. 169-188.
- [12] Raghavan, M. L., Vorp, D. A., Federle, M. P., Makaroun, M. S. and Webster, M. W., 2000, "Wall stress distribution on three-dimensionally reconstructed models of human abdominal aortic aneurysm," *J. Vasc. Surg.*, 31(4), pp. 760-769.

- [13] Shaaban, A. M. and Duerinckx, A. J., 2000, "Wall shear stress and early atherosclerosis: a review," *Am. J. Roentgenol.*, 174(6), pp. 1657-1665.
- [14] De Tullio, M.D., Cristallo, A., Balaras, E. and Verzicco, R. , 2009, "Direct numerical simulation of the pulsatile flow through an aortic bileaflet mechanical heart valve," *J. Fluid. Mech.*, 622, pp. 259-290.
- [15] Arzani, A. and Shadden, S.C., 2018, "Wall shear stress fixed points in cardiovascular fluid mechanics," *J. Biomech.*
- [16] Meierhofer, C., Schneider, E.P., Lyko, C., Hutter, A., Martinoff, S., Markl, M., Hager, A., Hess, J., Stern, H. and Fratz, S., 2012, "Wall shear stress and flow patterns in the ascending aorta in patients with bicuspid aortic valves differ significantly from tricuspid aortic valves: a prospective study," *Eur. Heart. J-Card. Img.*, 14(8), pp. 797-804.
- [17] Piatti, F., Sturla, F., Marom, G., Sheriff, J., Claiborne, T.E., Slepian, M.J., Redaelli, A. and Bluestein, D., 2015, "Hemodynamic and thrombogenic analysis of a trileaflet polymeric valve using a fluid–structure interaction approach," *J. Biomech.*, 48(13), pp. 3650-3658.
- [18] Vasava, P., Jalali, P. and Dabagh, M., 2009, "Computational Study of Pulstile Blood Flow in Aortic Arch: Effect of Blood Pressure," In *World Congress on Medical Physics and Biomedical Engineering*, September 7-12, 2009, Munich, Germany., pp. 1198-1201.
- [19] Shahcheraghi, N., Dwyer, H.A., Cheer, A.Y., Barakat, A.I. and Rutaganira, T., 2002, "Unsteady and three-dimensional simulation of blood flow in the human aortic arch," *J. Biomech. Eng.*, 124(4), pp. 378-387.
- [20] Triep, M., Hess, D., Chaves, H., Brücker, C., Balmert, A., Westhoff, G. and Bleckmann, H., 2013, "3D flow in the venom channel of a spitting cobra: do the ridges in the fangs act as fluid guide vanes?," *PloS one.*, 8(5), p. e61548.
- [21] Kim, T., Cheer, A.Y. and Dwyer, H.A., 2004, "A simulated dye method for flow visualization with a computational model for blood flow," *J. Biomech.*, 37(8), pp. 1125-1136.
- [22] Fung, Y.C., 2013, "Biomechanics: mechanical properties of living tissues," Springer Science & Business Media.
- [23] Clauser, J., Knieps, M.S., Büsen, M., Ding, A., Schmitz-Rode, T., Steinseifer, U., Arens, J. and Cattaneo, G. , 2018, "A Novel Plasma-Based Fluid for Particle Image Velocimetry (PIV): In-Vitro Feasibility Study of Flow Diverter Effects in Aneurysm Model," *Ann. Biomed. Eng.*, pp. 1-8.

- [24] Brücker, C., Steinseifer, U., Schröder, W. and Reul, H., 2002, "Unsteady flow through a new mechanical heart valve prosthesis analysed by digital particle image velocimetry," *Meas. Sci. Technol.*, 13(7), p. 1043.
- [25] Haller, G. and Sapsis, T., 2011, "Lagrangian coherent structures and the smallest finite-time Lyapunov exponent. *Chaos*," *An Interdisciplinary Journal of Nonlinear Science.*, 21(2), p. 023115.
- [26] Brücker, C., Spatz, J. and Schröder, W., 2005, "Feasability study of wall shear stress imaging using microstructured surfaces with flexible micropillars," *Exp. Fluids.*, 39(2), pp. 464-474.
- [27] Brücker, C., Bauer, D. and Chaves, H., 2007, "Dynamic response of micro-pillar sensors measuring fluctuating wall-shear-stress," *Exp. Fluids.*, 42(5), pp. 737-749.
- [28] Dickinson, B.T., Singler, J.R. and Batten, B.A. , 2012, "Mathematical modeling and simulation of biologically inspired hair receptor arrays in laminar unsteady flow separation," *J. Fluid. Struct.*, 29, pp. 1-17.
- [29] Kundu, P.K., Cohen, I.M. and Dowling, D.R., 2012, "Fluid Mechanics."
- [30] Stalder, A. F., Frydrychowicz, A., Russe, M. F., Korvink, J. G., Hennig, J., Li, K. and Markl, M., 2011, "Assessment of flow instabilities in the healthy aorta using flow - sensitive MRI," *J. Magn. Reson. Imaging.*, 33(4), pp. 839-846.
- [31] Lantz, J., Renner, J. and Karlsson, M., 2011, "Wall shear stress in a subject specific human aorta—influence of fluid-structure interaction," *Int. J. Appl. Mech.*, 3(04), pp. 759-778.

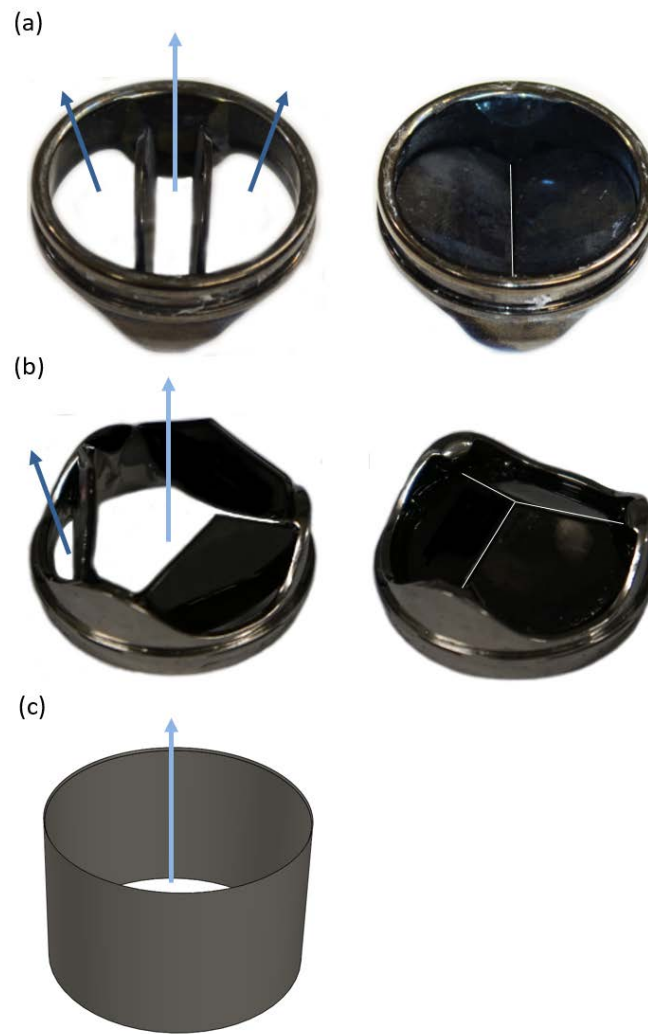


Fig. 1. (a) SJM Regent BMHV, with the leaflets in fully opening position (opening angle: 85°) and in the closed position (closed angle 25°). The valve generates a central orifice jet (light blue) and two side orifice jets (dark blue), which passes the heart valve between the valve ring and its leaflet. (b) Triflo TMHV, with the leaflets in fully opening position (opening angle: 75°) and in the closed position (closed angle 40°). The valve generates a central orifice jet (light blue) and side orifice jets (dark blue), which passes the heart valve between the valve ring and its leaflet. (c) Thin-walled nozzle with circular orifice.

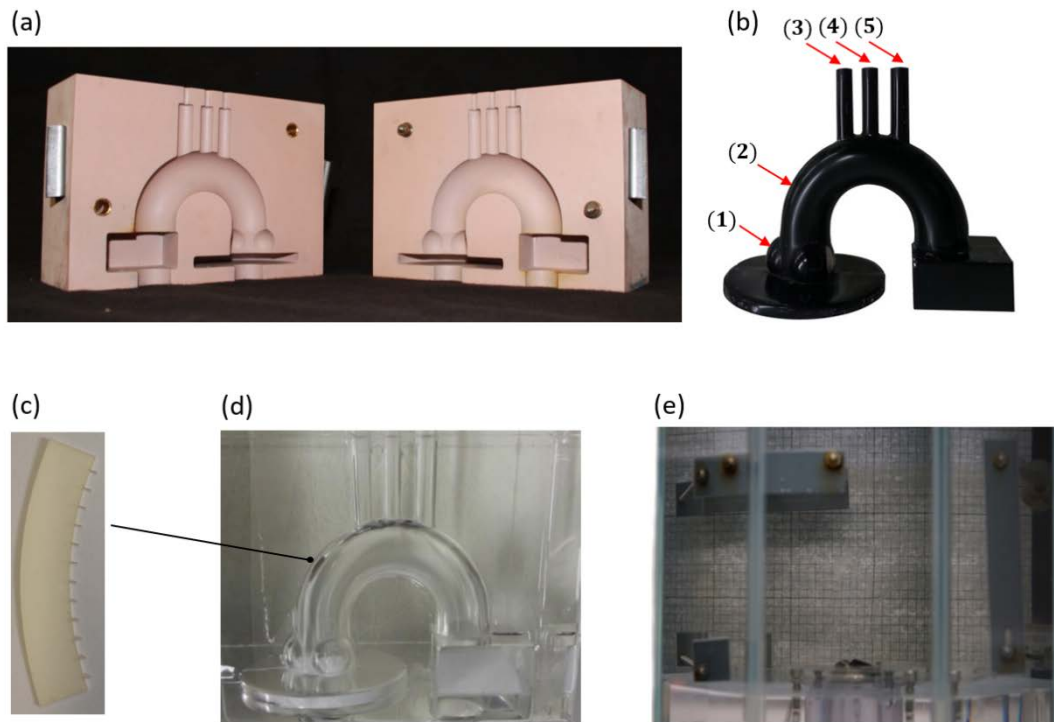


Fig. 2. Fabrication of the transparent silicone model of the aorta. (a) Mould for casting the negative form of the aorta. (b) Negative form of the aorta. Labelled locations are crossreferenced to dimensions of the aorta model shown in table 1. (c) The micro-pillar sensors carried by a thin sheet. (d) Assembled transparent silicon model of the aorta (Elastosil RT 601™) out of two halves. (e) Side view of the fluid basin. Refractive index matching of the transparent silicon model and the water-glycerine solution to verify the absence of optical distortion for flow imaging.

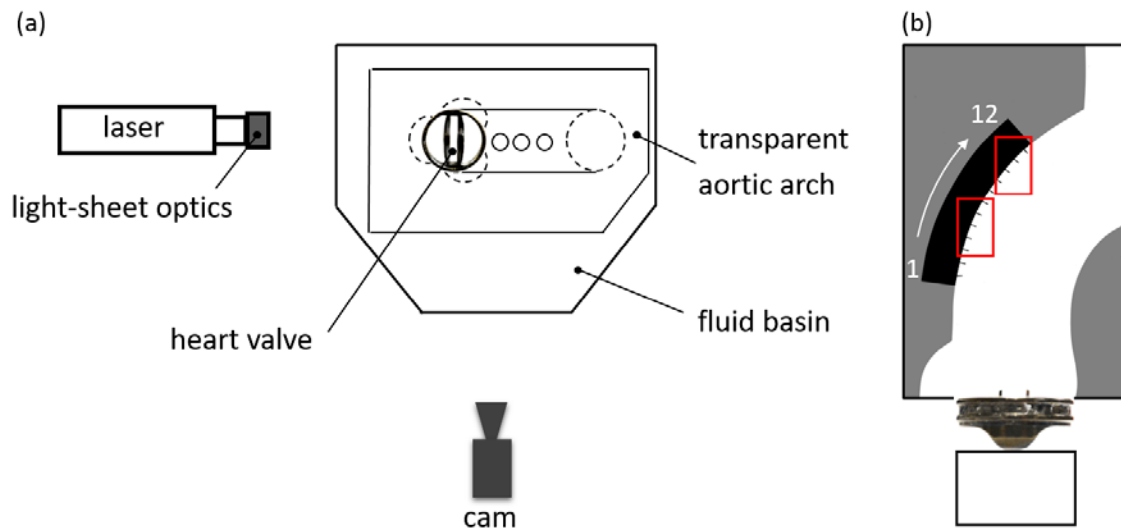


Fig. 3. (a) Schematic top view of the experimental set-up: the laser illuminates a thin plane in the middle of the aortic arch. The glass tank was filled with a water-glycerine solution to ensure the refractive index matching between the transparent aortic model and the fluid. (b) Schematic view of the different visualisation regions. Full AAO (the black rectangle downstream of MHV): $46 \times 73.7 \text{ mm}^2$. Zoom-in region (red rectangle): $4.0 \times 6.4 \text{ mm}^2$. Inlet flow measurement region (the black rectangle upstream of MHV): $25 \times 11 \text{ mm}^2$. PDMS sheet with micro-pillars is shown in black.

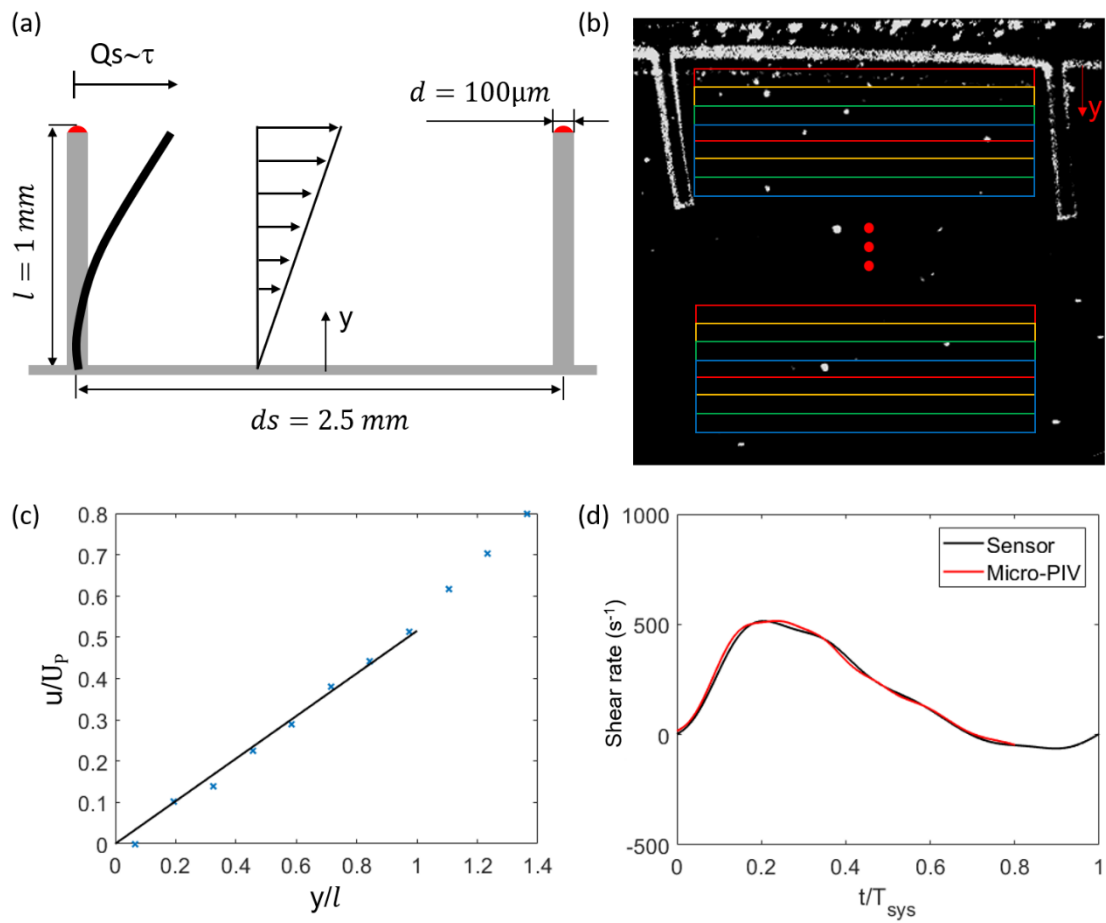


Fig. 4. (a) Parameters and the working principle of the micro-pillar sensors. (b) The sketch of the micro-PIV data processing. The cross-correlation window is presented by the coloured rectangles with 75% overlap of adjacent windows. (c) Plots of near wall velocity measured by the micro-PIV with blue marks and liner curve-fit. (d) Comparative plots of wall shear rate distribution over the systolic cycle.

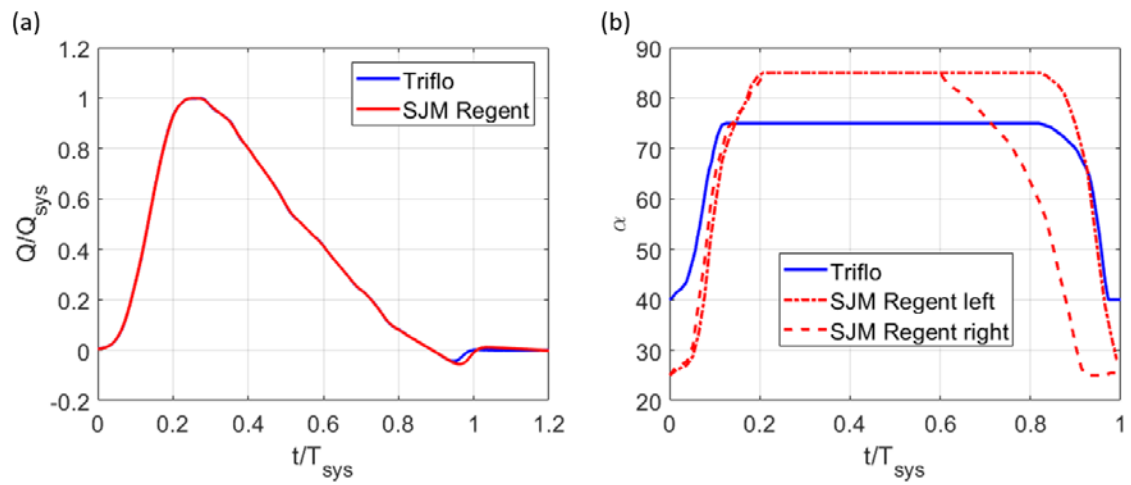


Fig. 5. (a) Inlet flow profile plotted by instantaneous non-dimensional mean inlet velocity measured at upstream of MHV over systolic cycle. (b) Profile of the motion of the leaflet's angular position over the systolic cycle. SJM Regent left marks the left leaflet of SJM Regent BMHV, while SJM Regent right marks the other leaflet. Triflo marks leaflets of Triflo TMHV.

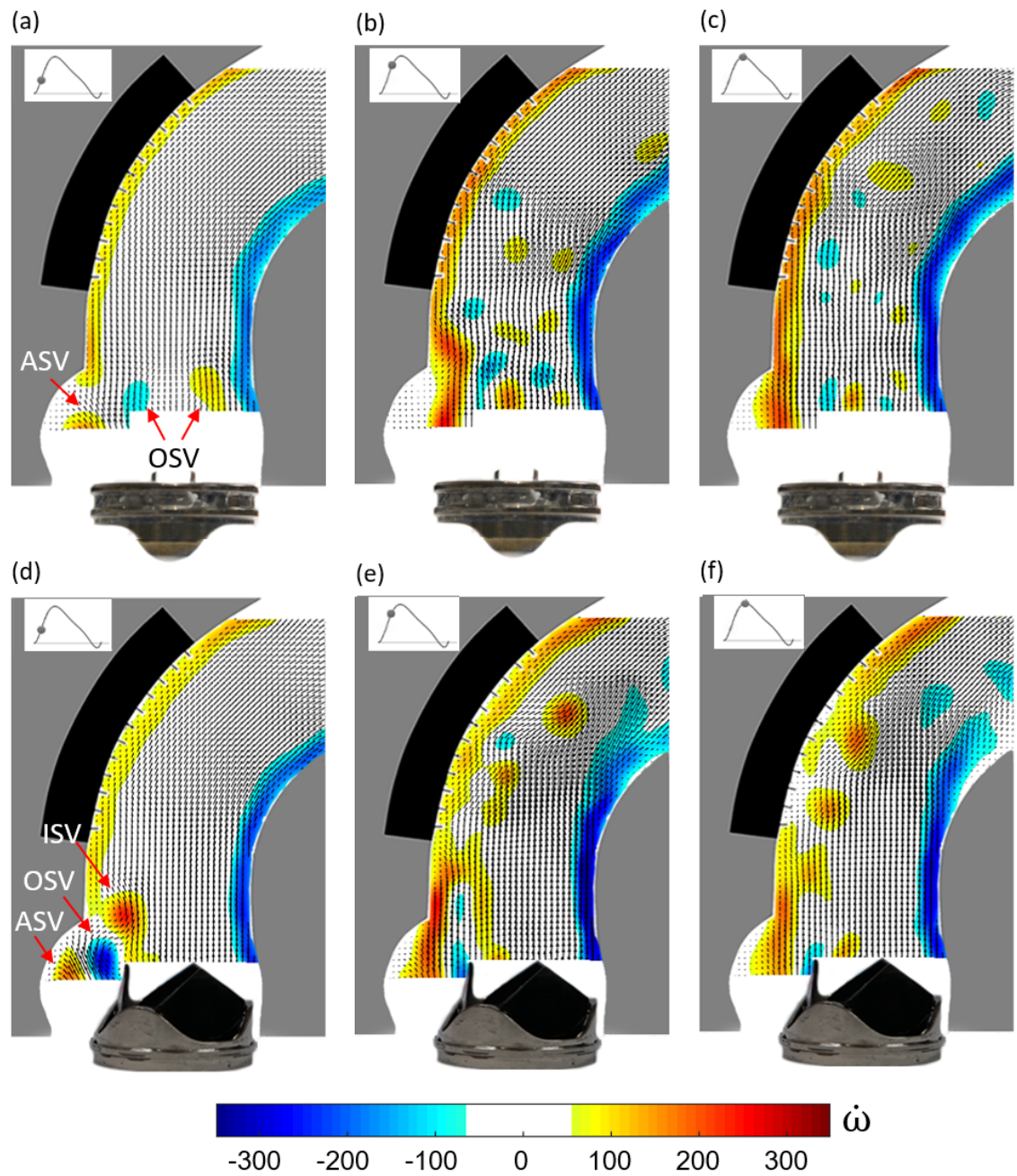


Fig. 6. Out-of-plane nondimensional vorticity $\hat{\omega}$ distribution overlaid on vector fields at (a) (d) $t/T_{sys} = 0.1$, (b)(e) $t/T_{sys} = 0.18$, (c)(f) $t/T_{sys} = 0.25$. OSV marks outer side (near the SOV) starting vortex. ISV marks inner side (near the centreline) starting vortex.

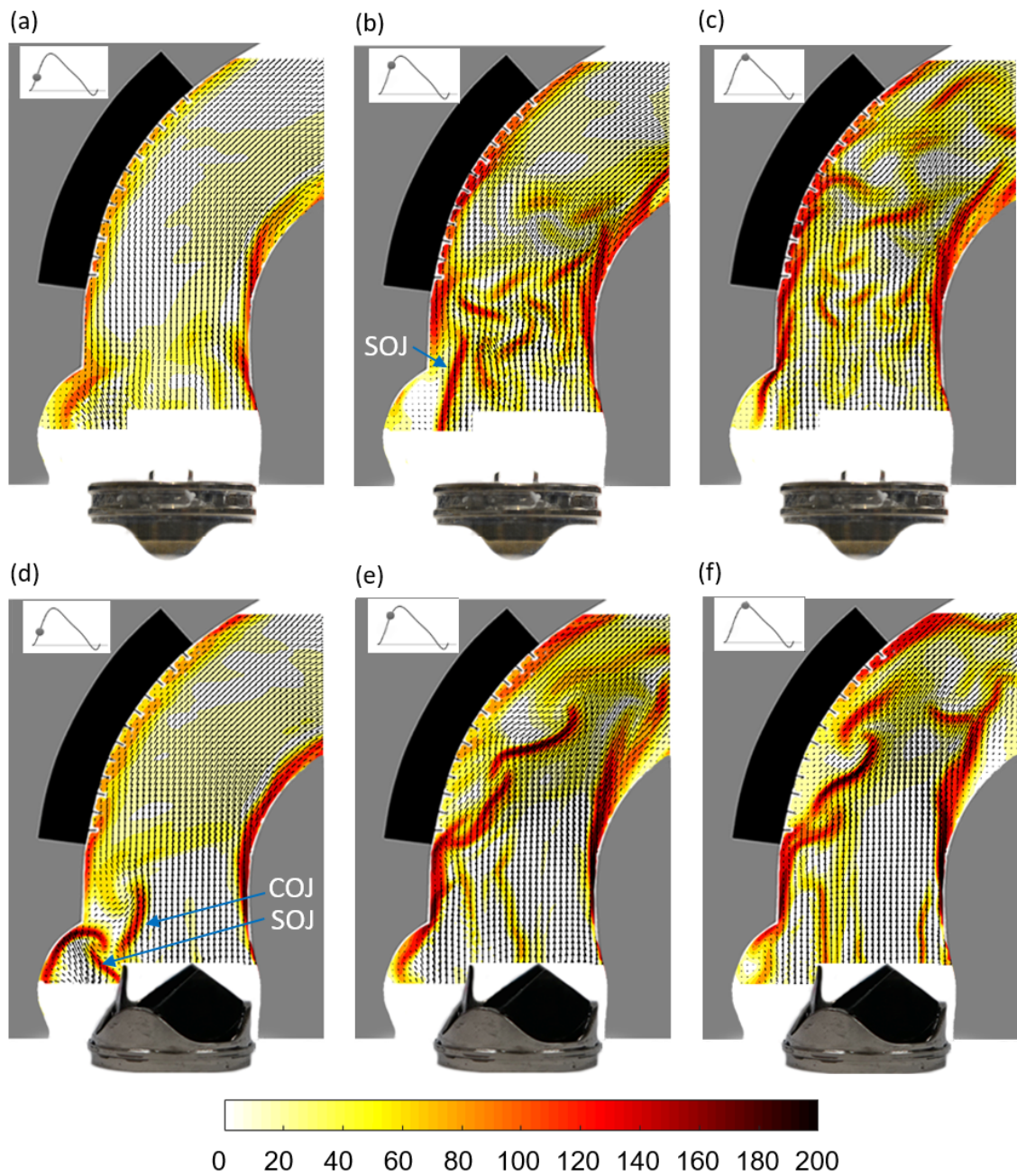


Fig. 7. Evolution of jet trajectories illustrated by the colored FTLE overlaid on snapshot vector fields at (a)(d) $t/T_{sys} = 0.1$, (b)(e) $t/T_{sys} = 0.18$, (c)(f) $t/T_{sys} = 0.25$. SOJ marks side orifice jet. COJ marks centre orifice jet.

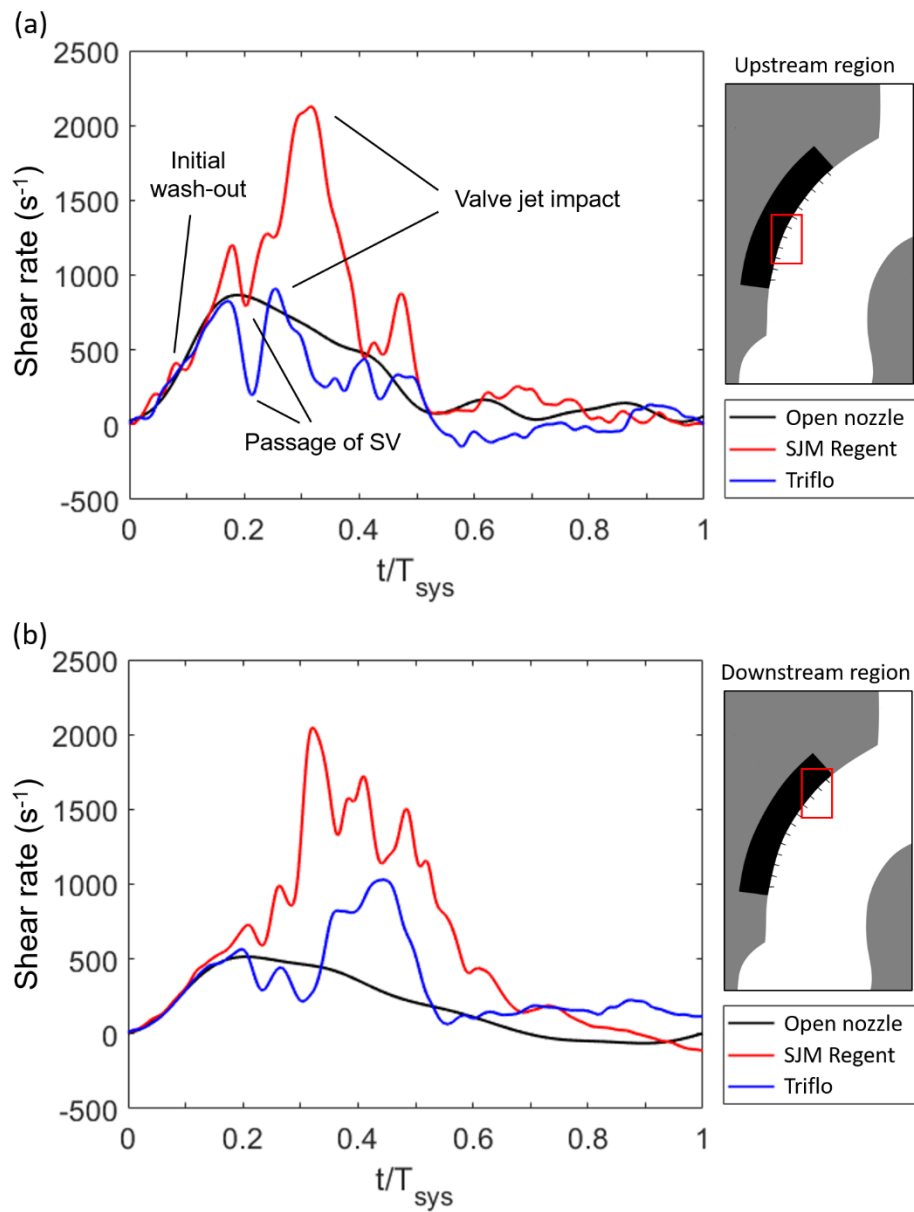


Fig. 8. Plots of wall shear rate distribution on (a) upstream region and (b) downstream region of the outer wall of the AAo over systolic cycle. Black line: open circular orifice nozzle, red line: SJM Regent BMHV, blue line: Triflo TMHV.